J. Eur. Opt. Society-Rapid Publ. 2022, **18**, 4
© The Author(s), published by EDP Sciences, 2022
https://doi.org/10.1051/jeos/2022003
Available online at: jeos.edpsciences.org

Journal of the European Optical Society-Rapid Publications

Atmospheric Plasma Jet processing for figure error correction of an optical element made from S-BSL7

Heike Müller[1,*], Thomas Waak[2], Uwe Birnbaum[2], Georg Böhm[1], and Thomas Arnold[1,3]

[1] Leibniz Institute of Surface Engineering (IOM), Permoserstraße 15, 04318 Leipzig, Germany
[2] JENOPTIK Optical Systems GmbH, Göschwitzer Straße 25, 07745 Jena, Germany
[3] Institute of Manufacturing Science and Engineering, TU Dresden, 01062 Dresden, Germany

Received 20 January 2022 / Accepted 15 June 2022

Abstract. To meet the increasing market demand for optical components, Plasma Jet Machining (PJM) of Borosilicate Crown Glass (BCG), which can be an alternative to Fused Silica, is presented. Surface figure error correction was performed by applying reactive plasma jet etching, where a fluorine-containing microwave driven plasma jet is employed to reduce the figure error in a deterministic dwell-time controlled dry etching process. However, some of the glass constituents of BCG cause the formation of a residual layer during surface treatment which influences the local material removal. By heating the substrate to about $T_S = 325$ °C to 350 °C during processing, the etching behavior can clearly be improved. Geometric conditions of the optical element nevertheless lead to a characteristic temperature distribution on the substrate surface, which requires an adjustment of the local dwell times in order to obtain the required material removal. Furthermore, the resulting local surface roughness is also influenced by the surface temperature distribution. It is shown that figure error can be significantly reduced by taking the local temperature distribution and resulting local etching rates into account. A subsequent polishing step smoothens roughness features occurring during etching to provide optical surface quality.

Keywords: Plasma Jet Machining, Atmospheric Plasma Jet, Reactive plasma jet etching, Borosilicate Crown Glass, Figure error, Chemical etching.

List of abbreviations

BCG	Borosilicate Crown Glass
FWHM	Full Width at Half Maximum
MRR	volumetric Material Removal Rate
OPD	Optical Path Difference
PJ	Plasma Jet
PJM	Plasma Jet Machining
PSD	Power Spectral Density function
WLI	White Light Interferometer

1 Introduction

An increasing automation of everyday processes requires further development of numerous optical devices, such as those needed for machine vision and laser technology. Human-machine interaction requires the ability of machines to visually record complex scenarios. Metrology is playing an increasingly important role in process monitoring and final inspection. Light is becoming a tool that is of great assistance in autonomous driving [1, 2]. All these technical achievements require the enlargement of the optical market in terms of its product breadth, but also in terms of low-cost optics with high imaging quality. One aspect regarding costs is the optical material used. Here, Borosilicate Crown Glass (BCG) represents a good alternative for visible and near-infrared applications. Being low-index glasses ($n_e \approx 1.52$) with high optical homogeneity, these exhibit very good transmission in a spectral range of about 380 nm to 1.8 µm (regarding thickness dependency) and can therefore be used as an alternative to Fused Silica to meet these requirements.

IOM has a high expertise in the field of ultra-precision figuring with plasmas and ions. Plasma Jet Machining (PJM) is a well-established technique for figuring and correcting various optical lens designs, such as spherical, aspherical and freeform lenses. The material variety, mainly

* Corresponding author: heike.mueller@iom-leipzig.de

This is an Open Access article distributed under the terms of the Creative Commons Attribution License (https://creativecommons.org/licenses/by/4.0), which permits unrestricted use, distribution, and reproduction in any medium, provided the original work is properly cited.

based on silicon, for instance Si, Fused Silica or SiC, is progressively extended to adapt to the market requirements [3–5].

Albeit, due to the chemical interactions between the reactive species generated in the plasma and the substrate material of optical glasses, various effects such as layer formation can occur, which influence the local etch rate and thus lead to inhomogeneous and difficult-to-predict material removal. However, for the application of the dwell time method, the exact knowledge of the local removal rate is crucial. Based on extensive fundamental research on plasma processing of N-BK7® the most famous representative of BCG, the influencing parameters were identified and measures to compensate nonlinear effects were developed [6, 7]. Hence, atmospheric pressure PJM of BCG is now to enable the production of optical elements with many degrees of freedom and meet ultra-precision manufacturing.

In the following, the workflow for PJM-based figure error correction of an optical element made of S-BSL7 glass is presented. Since surface temperature plays a major role in the chemically driven plasma etching process which significantly affects material removal rate and surface roughness, a careful assessment of the main influencing parameters or their local distribution functions like local surface temperature and etching rate function depending on substrate heater temperature, natural convection, plasma power, and local dwell time has been undertaken. Such parameters and functions are then introduced into the process simulation in order to calculate local dwell times for the machining process. Preliminary tests show the feasibility of this approach. Finally, the successful correction of an optical element made of S-BSL7, and the achievement of optical surface quality is demonstrated.

2 Experimental

The principle of PJM was developed at the IOM about two decades ago. Since then, the Plasma Jet (PJ) source has been continuously improved to meet current research purposes and material requirements. A schematic drawing of the PJ source used in this work can be seen in Figure 1. It is based on a coaxial conductive system where the reactive gas carbon tetrafluoride (CF_4) and helium (He), acting as inert carrier gas, are supplied through the central gas inlet made from copper. Furthermore, oxygen (O_2) is added through this inner conductor, which causes the fluorine radical yield to increase [8], thereby increasing the material removal rate. Furthermore, the addition of O_2 prevents the formation of fluorocarbon films on BCG [9]. The shielding gas nitrogen (N_2) is passed through the outer brass electrode enabling the generation of a locally stable plasma jet discharge. The PJ source is mounted on a 3-axis-CNC motion system to perform a scanning motion scheme over the substrate, usually a meander path where the lines are directed along the x-axis and the line feed is executed along the y-axis.

A microwave generator (PP3030, *Trionplas Technologies GmbH*) coupled *via* a coaxial cable to the PJ source provides microwave power to plasma nozzle where the gas mixture is excited by a high-frequency electric field. Pulsed microwave of 2.45 GHz with peak power of 250 W, pulse frequency of approx. 1 kHz and pulse length of approx. 10 μs propagates along the inner electrode. A mean power of 10 W to 20 W can be adjusted by varying the pulse frequency. The ignition of the gas discharge at the nozzle tip occurs as soon as the intensity of the electric field intensity exceeds the breakdown intensity and at least one free electron is present. In the excited gas flow, dissociation and recombination of the CF_4 molecules occur. The fluorine radicals react with the silicon-containing substrate forming gaseous compounds, which lead to material removal. In the case of Fused Silica (SiO_2), only volatile components such as SiF_4 and CO_2 are formed. For substrates containing additional components like BCG, individual considerations of their surface reactions must be made, as further glass constituents strongly influence the etching behavior during plasma jet processing.

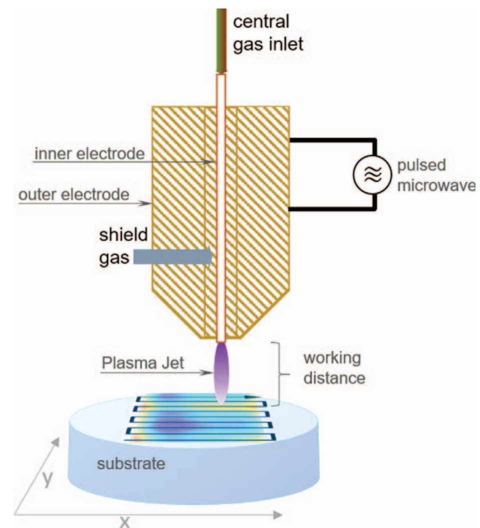

Fig. 1. Schematic drawing of PJ source.

3 Material and measurements

Due to their low refractive index ($n_e = 1.52$) and low dispersion ($\nu_e = 63.93$), crown glasses are commonly used for optical elements applied in visible and near-infrared spectra. BCG is defined as a type of crown glasses consisting of approx. 60–70% SiO_2 and at least 10% of boron oxide among other metal oxide constituents. As a result, such glasses are characterized by high mechanical hardness and chemical resistance. Several fundamental studies on the plasma jet figuring of N-BK7® made by *Schott AG* have been performed in recent years [6–10]. The chemical composition of the material and the interaction effect of the fluorine containing reactive PJ on the formation of a residual layer were investigated for glass surfaces at room temperature [9] but also for heated substrates to elevated temperatures [10]. It was shown that pre-heating of the sample to approx. T_S = 350 °C is necessary to obtain a Gaussian etching

Table 1. Nominal chemical composition of S-BSL7 compared to N-BK7®.

Component	Proportion of S-BSL7 (%) (*Ohara GmbH*)	Proportion of N-BK7® (%) (*Schott AG*)
SiO_2	60–70	60–70
B_2O_3	10–20	10–20
BaO	0–2	1–10
ZnO	0–2	–
Sb_2O_3	0–2	<1
TiO_2	0–2	<1
Na_2O	–	10–20
K_2O	–	1–10
CaO	–	<1
Cl_2	–	<1

profile instead of an irregularly shaped profile. In this case the morphology of the residual layer changes from dense structure exhibiting cracks to a homogeneous porous structure which allows a more uniform etch attack of the reactive species to the glass phase. Thus, the thermal treatment leads to a significant reduced micro-roughness compared to PJ etching at room temperature [10]. The development of residual layer thickness was described using the Deal–Grove model [6]. It was further shown that the etching rate is mainly determined by the surface temperature and, to a minor extend, by the local residual layer thickness [6]. The deduced model for non-linear local etch rates was then employed in an extended iterative dwell time calculation algorithm [7]. Based on the findings so far, the current study of figure error correction of an optical element made of BCG was performed.

Since the various BCG differ slightly in their composition the investigations of N-BK7® cannot be fully used for the processing of S-BSL7 glass. Minor adjustments in etching behavior are to be expected due to the variation of the components. Table 1 compares the components taken from the material safety data sheet of S-BSL7 [11], the BCG of *Ohara GmbH*, with those of N-BK7® [12].

It was shown that PJ etching of BCG using fluorine-containing gas, such as CF_4, results in the formation of fluorides. Their individual boiling point determines whether the reaction products form volatile compounds or solid material. The chemical equations and boiling points of the components involved can be found in Table 2. SiO_2 and B_2O_3 form volatile gases in combination with fluorine at room temperature. Hence, these products lead to the material removal. The remaining components, which make up a small proportion of the total mixture, form solid fluoride compounds which remain as a layer on top of the surface and thus influence the etching process. It has been shown that performing a plasma etching process at elevated surface temperatures of approx. 350 °C seems to be beneficial for etching homogeneity and improves the stability of the etching rate [10]. Hence, in the following experiments the samples are heated by an external hotplate during processing.

The dimensions of the optical element made from S-BSL7 which is to be corrected are shown in Figure 2. The acylindrical element has a concave curvature along the longer dimension (which is designated as x direction) with total length of 230 mm resulting in a height difference (sag) of 9.024 mm. The width of the workpiece in y direction is 35 mm, where no curvature is found in this direction. The varying sample thickness poses a challenge to the temperature treatment, since the fundamental studies of Kazemi *et al.* [6–10], which has been described in the section before, were always performed on planar thin samples of 3 mm thickness.

Etching tests prior to the processing of the optical element were performed on smaller round S-BSL7 glass samples with a diameter of 18 mm and a thickness of 9 mm exhibiting a planar polished surface. With these test samples the plasma process parameters were optimized and the effects of the PJ scan velocity and local surface temperatures on the etching rate were investigated.

In order to remove any surface contamination or particles that could affect the etching results, the samples were cleaned in an ultrasonic bath prior to processing. After PJ etching, the samples were cooled slowly. Then again, they were ultrasonic cleaned to remove the residual layer before performing surface measurements.

For PJM the test samples as well as the optical element are placed on a substrate heater in the CNC machine which enables to heat up the glass substrates to temperatures up to 600 °C.

The heating and cooling behavior of the samples were determined by IR-thermography using an IR camera (PI160, *Optris GmbH*) mounted on the motion system. This camera is pointed at the contact zone of the PJ and the substrate. Furthermore, the camera is installed in such a way on the motion system that it follows the line feed in the y-direction. In x-direction, the PJ passes through the measuring point when executing a line scan. Thus, in addition to the determination of the temporal trend of the full sample surface heating during processing the current temperature in the contact zone could be observed. The emissivity of the glass substrate was adjusted to $\varepsilon = 0.8$ by temperature comparison of a sooted and a bare glass surface where the emissivity on the sooted area was assumed to be $\varepsilon = 0.95$ [15].

To determine the material removal of the round test samples, the processed substrates were measured using a non-contact optical surface profiler (LuphoScan 260HD,

Table 2. Chemical equations and boiling points of the alkalifluorides occuring while plasma etching of BCG with CF_4.

Component	Proportion (%)	Chemical reaction	Boiling points
SiO_2	60–70	$SiO_2 + CF_4 \rightarrow SiF_4 + CO_2$	−95.2 °C subl. [13]
B_2O_3	10–20	$2B_2O_3 + 3CF_4 \rightarrow 4BF_3 + 3CO_2$	−101 °C [14]
BaO	0–2	$2BaO + CF_4 \rightarrow 2BaF_2 + CO_2$	2260 °C [14]
ZnO	0–2	$2ZnO + CF_4 \rightarrow 2ZnF_2 + CO_2$	1500 °C [14]
Sb_2O_3	0–2	$2Sb_2O_3 +3\ CF_4 \rightarrow 4SbF_3 + 3CO_2$	345 °C [14]
		$Sb_2O_3 + CF_4 + 8F^- \rightarrow SbF_5 + CO_2$	141 °C [14]
TiO_2	0–2	$TiO_2 + CF_4 \rightarrow TiF_4 + CO_2$	284 °C subl. [14]
		$TiO_2 + CF_4 \rightarrow TiF_3 + CO_2 + F^-$	1400 °C [14]

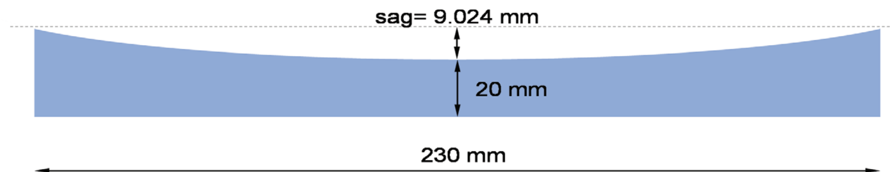

Fig. 2. Cross-section of the optical element with indication of the main dimensions.

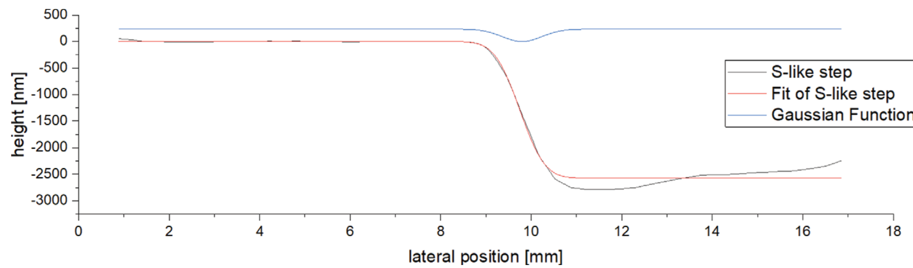

Fig. 3. Measurement of the S-like step after etching semicircle area for computation of the PJ etching parameters.

Taylor Hobson Ltd.). By deconvolution of the S-like step (see Fig. 3) occurring after etching a semicircle area the parameters of the PJ etch rate function were computed. Here, a Gaussian function was assumed characterized by the Full Width at Half Maximum (FWHM). The volumetric Material Removal Rate (MRR) was calculated by

$$\mathrm{MRR}\ = h \cdot v \cdot \Delta y, \quad (1)$$

where h is the height of the S-like step, v is the PJ scan velocity and Δy expresses the line feed of the processed area.

The figure error of the optical element was determined based on an area measurement using the non-contact profilometer (CT350S, *Cyber Technologies GmbH*). By matching with the nominal surface design, the figure error was calculated.

Surface roughness was evaluated by White Light Interferometry (WLI, NPFLEX, *Bruker Corporation*) using different objectives. With the help of a Matlab® script, a combined isotropic Power Spectral Density (PSD) function was calculated from the individual measurements covering a total spatial wavelength range of approx. 1.1×10^{-3} µm^{-1} to 2 µm^{-1}.

The occurrence of birefringence induced by internal stress was observed using the StrainScope S3/180 (*ilis GmbH*). In accordance with the conventions of optical technologies, the values of the Optical Path Difference (OPD) were normalized to the thickness of the samples.

To determine the basic etching behavior, five test samples were evenly distributed on a sample holder, which in turn was positioned on the heater. By arranging those samples, five different scan velocities of the PJ could be tested in one heating cycle. Semicircle areas were etched applying a meander path with constant velocities (1, 2, 4, 8, 16 mm/s). The radius of the area was 10 mm, and the line feed was 0.1 mm.

Figure error correction was performed based on the dwell-time method. The usual mathematical description for the relationship between etching depth, tool function and dwell time can be expressed as follows: $h_{ij} = R \times t_{ij} + \varepsilon$. In order to obtain the dwell time matrix t_{ij}, deconvolution of the topography of the figure error, represented by a discrete height matrix h_{ij}, with the tool function R approximated by a rotationally symmetric Gaussian function is performed. Additionally, the theoretical residual error ε is obtained. For the purpose of PJ etching a dedicated

Table 3. Indication of the surface temperatures resulting from the preset heater temperatures without heat impact of the PJ.

Heater temperature T_H (°C)	Surface temperature T_S (°C)
400	275
500	325
600	370

numerical deconvolution algorithm was employed over the last decades. Besides other specific features it is able to account for variable local etch rates. Finally, the dwell time matrix t_{ij} is transferred to local velocities, considering the tool path and the machine kinematics, and provided as CNC data for machining.

4 Results

4.1 Optimization of etching behavior of S-BSL7

For a successful application of PJM on S-BSL7 process parameters have to be optimized in terms of maximum material removal rate, minimum surface roughness, and minimum birefringence ensuring minimum processing time and high optical performance of the optical element. In order to investigate the etching behavior of the substrate material S-BSL7, first the influence of the surface temperature is considered, which is mainly achieved by external sample heating.

Kazemi *et al.* investigated the influence of surface temperature in detail [10]. They found that increasing the surface temperature enables less masking due to non-volatile products that are deposited on the surface. The residual layer becomes less dense and the increasing porosity ensures that this layer is permeable to the reactive species generated in the PJ. In this case the footprint of the PJ is Gaussian-like [10]. Following these investigations on N-BK7®, surface temperatures T_S between 300 °C and 400 °C were initially targeted [10]. The heater temperatures and resulting surface temperatures of the presented experiments can be taken from Table 3.

The surface temperatures result from the equilibrium of heat flow from the sample heater as heat source and natural convection of ambient air as heat sink. For these measurements, the PJ was not yet in contact with the sample surface.

For the determination of the material removal rate depending on different surface temperatures as well as for varying scan velocities of the plasma jet the microwave power was set to 10 W. The central gas inlet was fed by $[He]$ = 200 sccm He, $[O_2]$ = 2 sccm O_2 and $[CF_4]$ = 1 sccm CF_4. The outer shield gas flow rate was adjusted to $[N_2]$ = 600 sccm N_2. The results are shown in Figure 4a. As the velocity increases the MRR decreases if the same heater temperature is considered. When comparing the same velocities, it is also obvious that the MRR increases as the heater temperature increases.

It is well known that the chemical reaction rates on the surface are mainly controlled by the Arrhenius law, which can be described by

$$\mathrm{MRR} \propto C\,j\,\exp\left(-\frac{E_A}{k_B T_S}\right) \tag{2}$$

where C contains material constants, j is the current density of reactive particles, E_A is an activation energy, and k_B is the Boltzmann constant. As PJ acts as an additional local heat source a longer PJ dwell time due to lower velocities provides a larger local heating which leads to an increase of the effective local surface temperature and consequently to an increase of the MRR.

It has been shown in previous plasma jet related work [16, 17] that the dependence of MRR on the velocity can be well approximated by an exponential decreasing function of the form

$$\mathrm{MRR} \propto a + b\,\exp(-v/c) \tag{3}$$

where a, b, and c are fitting parameters. In Figure 4b the normalized MRR is plotted *versus* the surface temperature disregarding the local heating of the PJ. Since the surface temperature range is relatively narrow, the MRR dependence on the initial surface temperature shows a near linear dependence instead of the functional form of equation (2). Two outliers were not taken into account in the linear fit since they belong to the scan velocity of v = 16 mm/s where the MRR is obviously overestimated due to very small etching depths.

In order to evaluate the surface quality after etching, surface roughness was measured. The results are shown in Figure 4c as a function of the resulting etching depth. Typical surface topographies for observed with the WLI are depicted in Figure 4e at T_H = 500 °C. It is known that the roughness of a glass surface (*e.g.* Fused Silica) usually increases with stronger etching attack due to sub-surface damage which develops and forms a characteristic roughness depending on the amount of material removal [16, 18, 19]. Fundamental studies on N-BK7® show a further effect of roughness development [10], which is attributed to partial masking of the formed layer on the surface preventing uniform etching. It is evident that the roughness is lower at higher temperature for comparable etching depths. It was shown previously that the morphology of the residual layer depends on the formation temperature. At surface temperatures less than 200 °C the layer is denser but exhibits many cracks leading to a high surface roughness when reactive species etch the glass at the cracks while the layer covered parts are masked out. When surface temperature is about 350 °C the layer has a more uniform and porous structure and no cracks are observed. Reactive particles can penetrate to some extend the layer and a more homogeneous etch attack proceeds [10].

Consequently, it can be concluded that the temperature of the heater should be selected high enough to enable low roughness. Here, however, the glass transition temperature has to be considered, which is T_G = 576 °C for S-BSL7. Even if the temperature does not reach this value at the surface, higher temperatures are achieved in direct contact

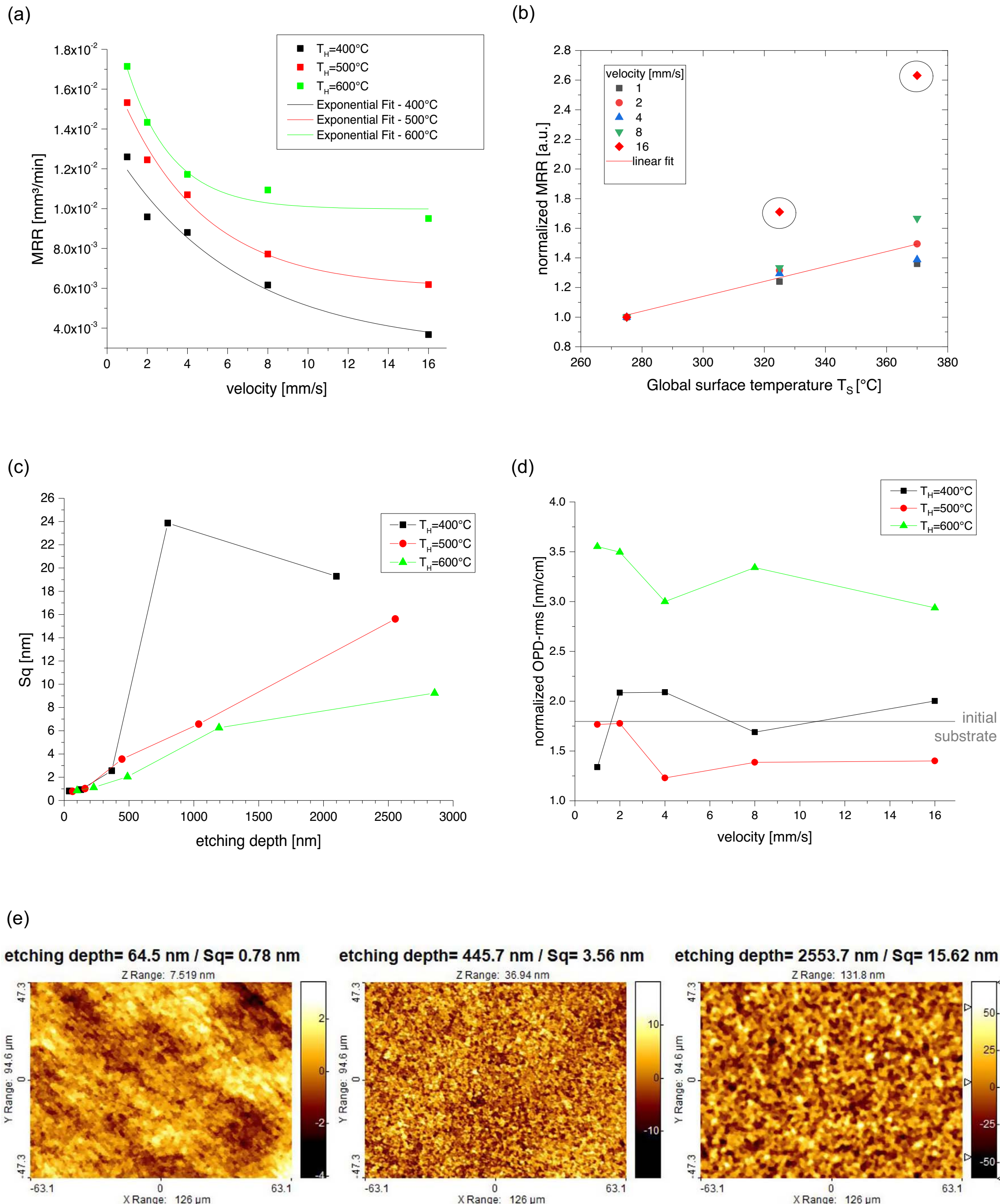

Fig. 4. Influence of different heater temperatures: (a) velocity dependent material removal rate, (b) normalized MRR at different surface temperatures T_S, the encircled outliers were not regarded in the linear fit, (c) roughness Sq, (d) birefringence specified as normalized optical path difference and (e) surface topographies representing various surface roughness due to increasing etching depths (T_H = 500 °C).

between the sample backside and the aluminum holder. Nonuniform heating of the glass can lead to birefringence which may deteriorate the optical performance of optics. Looking at the birefringence shown in Figure 4d, it is noticeable that the RMS-value of the normalized optical path difference for heater temperatures up to 500 °C is in the range of the initial sample (norm. OPD-rms = 1.796 nm). However, tests at a heater temperature of T_H = 600 °C reveal higher OPD values in the substrate. Hence, too high substrate temperatures should be avoided for optics machining.

Based on the results obtained so far, a heater temperature of T_H = 500 °C (*i.e.* a global surface temperature of T_S = 325 °C) was used to perform further investigations

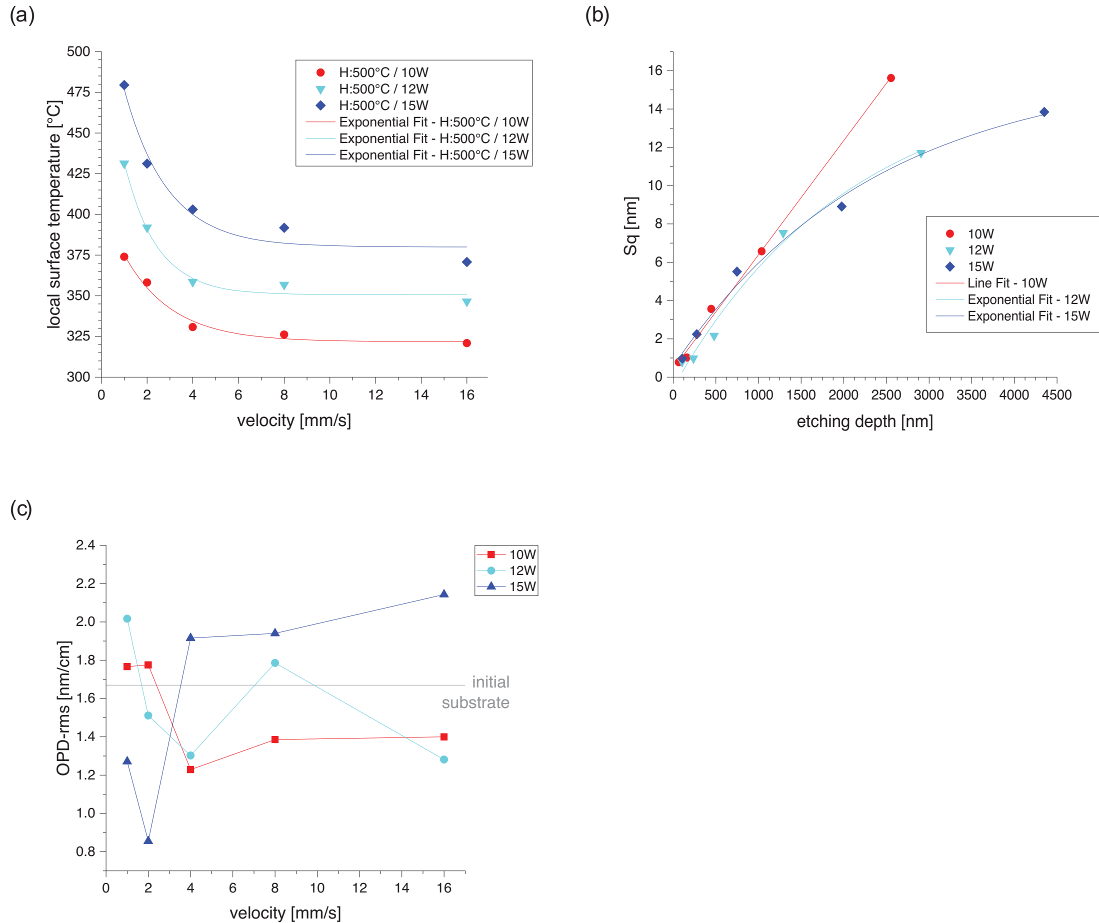

Fig. 5. (a) Surface temperatures during PJ machining at different velocities applying different microwave power, (b) influence of different microwave power on roughness Sq and (c) birefringence specified as normalized optical path difference.

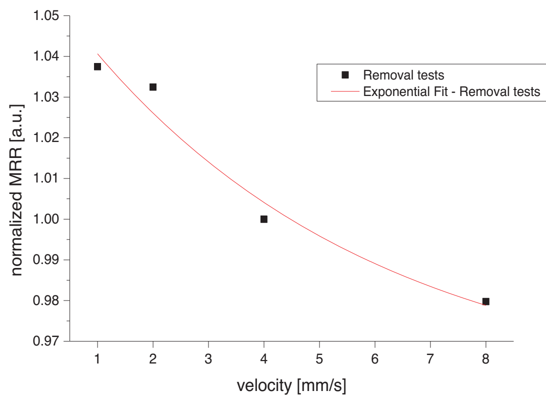

Fig. 6. Dependency of MRR normalized to the value at $v = 4$ mm/s on scan velocity of the PJ having a working distance of 3.5 mm (process parameters: [He] = 200 sccm, $[O_2]$ = 2 sccm, $[CF_4]$ = 1 sccm, $[N_2]$ = 600 sccm, P = 15 W, T_H = 500 °C).

on the influence of applied microwave power. For these tests, mean power levels of 12 W and 15 W were adjusted to compare the etching results with those obtained at 10 W using the same experimental setup. In order to better assess the effect of increasing microwave power, local surface temperatures during processing were measured, which are depicted in Figure 5. Obviously, a higher power leads to a higher local surface temperature on the substrate, and consequently higher MRR are achieved.

The roughness Sq, measured with the 50× objective, shows a nearly linear dependence on the resulting etching depth for 10 W (see Fig. 5b). At increased microwave power, no significant difference in the depth dependence can be observed. At both 12 W and 15 W, roughness appears to depend according to a power law on etching depth. This behavior correlates with the roughness measurement at elevated heater temperature of 600 °C shown in Figure 4c. Obviously, the local surface temperature is determining the depth dependent roughening. For all three microwave powers investigated, no significant difference in the occurrence of birefringence can be seen. The OPD-rms values shown in Figure 5c indicate a statistical distribution around the OPD value of the initial substrate.

The investigations show that for a power level of 15 W a reasonable roughness and no significant rise of birefringence is obtained. Hence, the following dwell time-controlled figure error correction process is performed at the power level of 15 W and 500 °C heater temperature.

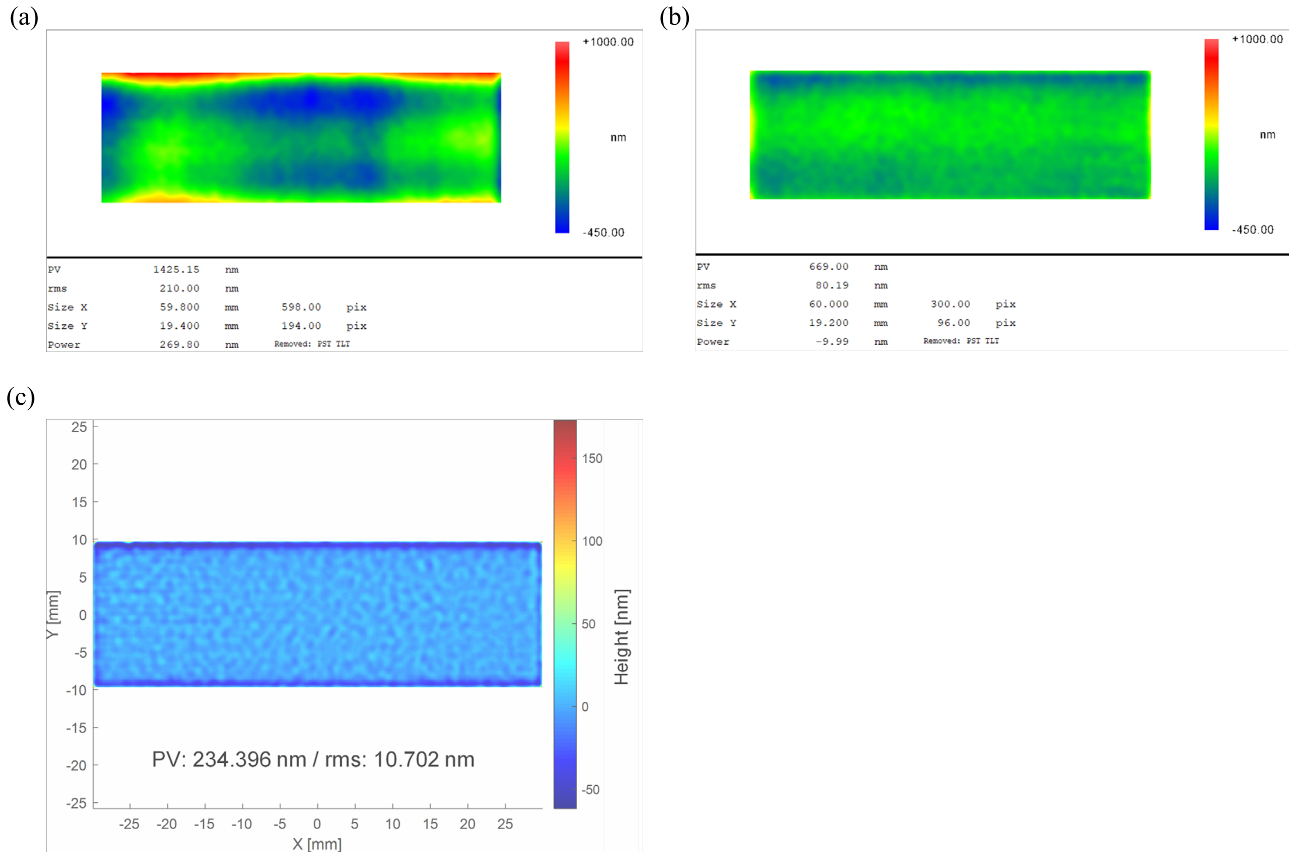

Fig. 7. Figure error correction on optical element: (a) figure error before and (b) after PJ machining, (c) compared to the theoretical figure error resulting from dwell-time calculation.

4.2 Figure error correction on optical element

A first figure error correction test was performed on a partial area of a test substrate heated to $T_\mathrm{H} = 500$ °C with the dimensions of the optical component shown in Figure 2. The origin of the coordinate system for PJM is located on the surface in the workpiece center. The selected area is located in the central part of the element and has a length of 60 mm, a width of 20 mm, and a height difference (sag) of 1.2 mm due to the curvature of the element.

The global surface temperature T_S measured with the IR camera is between 300 °C and 325 °C. To take the velocity dependence of the MRR into account, the normalized etching rates given in Figure 6 were approximated by an exponential function and implemented in the dwell time calculation algorithm.

Figures 7a and 7b show the surface measurement of the partial area before and after figure error correction. The areal figure error was reduced from 210.00 nm rms to 80.19 nm rms. The theoretical residual figure error shown in Figures 7c could not be reached but the planarization of the long-wave error and the reduction of the initial figure error by 62% is evident.

To determine the roughness, the sample was measured by WLI at three random measurement points after correction. Figure 8 shows the isotropic PSD. No distinct

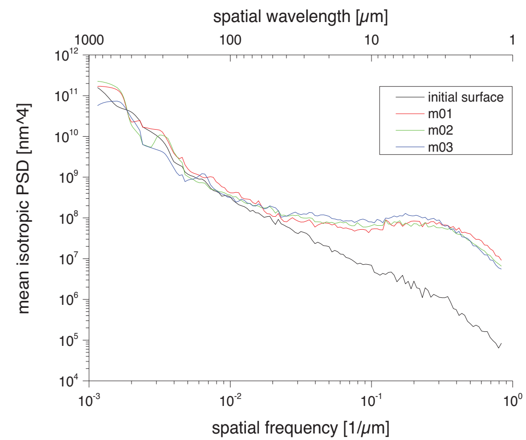

Fig. 8. Isotropic PSD determined at three random points compared to initial surface.

differences occur among the individual measuring points. The roughness increases steadily starting at a spatial frequency of 10^{-2} $\mu\mathrm{m}^{-1}$. Hence, for achieving optical quality the roughness must be further reduced by additional processing steps *e.g.* by polishing.

Although the previous result is promising, a measurement of the surface temperature of the entire surface of

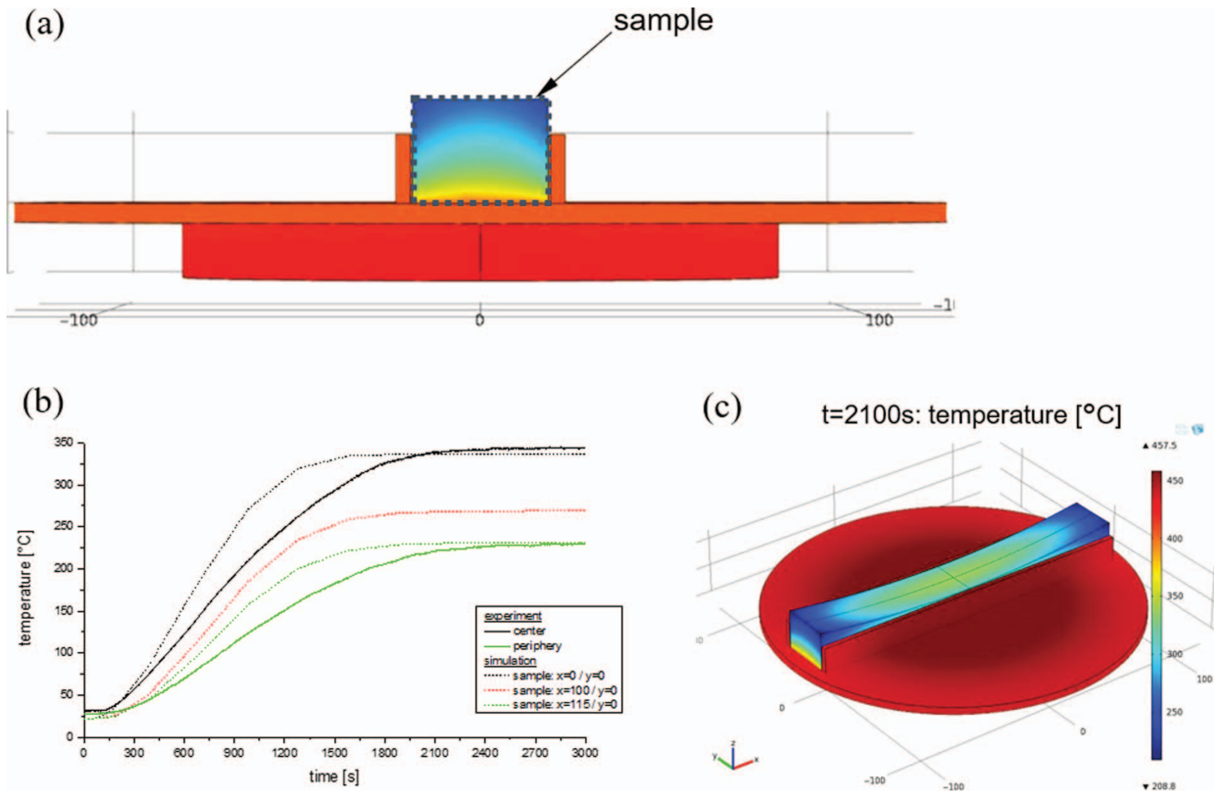

Fig. 9. Model for thermal FEM simulation: (a) fixation of the sample on mounting plate (yz view), (b) comparison of measured and simulated heating-up curves for different x positions on the optical element, (c) stationary temperature distribution after $t = 2100$ s.

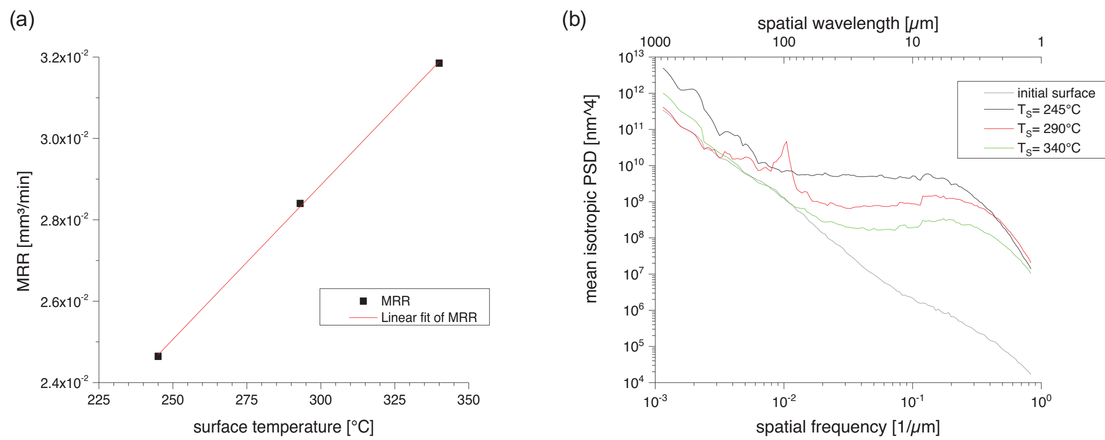

Fig. 10. Influence of different surface temperatures on (a) MRR and (b) isotropic PSD (process parameters: 15 W, $v = 4$ mm/s).

the optical element reveals a non-uniform temperature distribution. This lateral distribution must be additionally considered in the dwell time calculation when the full surface is to be processed, as it influences the MRR. A characteristic local temperature distribution originates from the dimensions of the heater and the workpiece holder setup. The optical element is mounted in a fixed position on the heater by using a sample holder. The combination of optics and mounting plate is shown in Figure 9a. The sample holder (shown in red and orange) is a plate made of aluminum, which is fixed on the heater. The sample is placed between two aluminum walls (height: 17.5 mm), which are supposed to reduce the convective heat loss through the sample side as much as possible.

Since the IR camera measurements on the curved surface are only estimates and may contain measurement errors due to varying angle of incidence the temperature of the sample surface was modeled using COMSOL® Multiphysics.

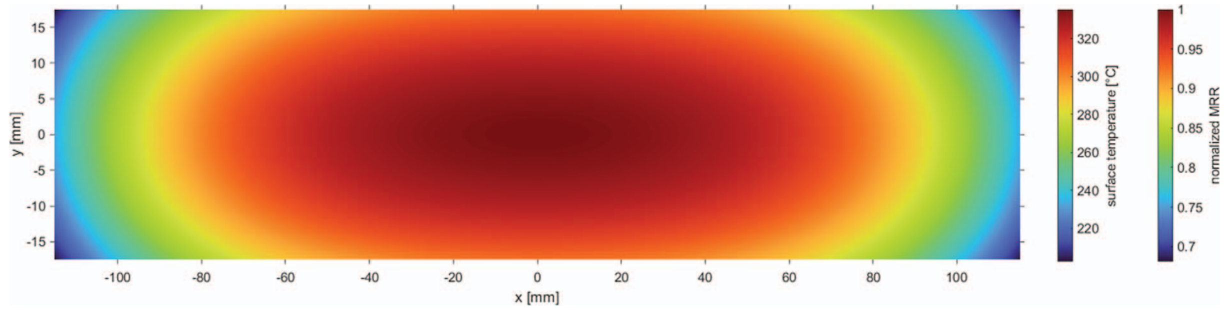

Fig. 11. Scaling of the MRR for dwell time calculation as a function of temperature resulting from geometry of the optical element.

The measured heater temperature (T_H = 500 °C) is taken as one boundary condition. Furthermore, convective cooling by the surrounding air is assumed. According to the real conditions, the bottom of the sample is in full contact with the sample holder, while are narrow air gaps of 0.1 mm are considered between the side walls and the sample.

In Figure 9b the surface temperature measured in the center and in the periphery is compared to the simulation. For the simulation, defined points on the specimen surface with $y = 0$ are selected. The position $x = 0$ describes the center of the sample, $x = 100$ mm the edge of the processed area and $x = 115$ mm the edge of the sample. Heating is slightly less intense during the experiment, which results in a longer heating time. Since the simulation is based on an ideal thermal connection between the sample and the sample holder, a time offset can be present in the experiment where the thermal contact might not be perfect. The heat conduction into the sample material therefore occurs more slowly than under the modelled conditions.

A stationary temperature distribution shown in Figure 9c is reached after approx. $t = 2100$ s. Measurement results and simulated temperatures correspond well.

A quantitative determination of the MRR depending on the surface temperature was performed on three test samples. Different surface temperatures (approximately: T_S = 245 °C/290 °C/340 °C) were adjusted to reflect the conditions of the optical element at different lateral positions. Figure 10a clearly illustrates the linear dependence of MRR on surface temperature that was already qualitatively shown in Figure 4b. This dependence must be considered when calculating the dwell times for figure error correction of the entire optical element.

In addition, the isotropic PSD compared to the initial surface for all three surface temperatures is given in Figure 10b. Similar to the previous investigations, a significant roughening for spatial frequencies higher than 10^{-2} μm^{-1} is observed. Furthermore, a temperature dependence becomes obvious. At a surface temperature of 245 °C, the sample roughens over the entire range considered. A vertical shift of the graph with respect to the initial surface can be seen. The more the sample is heated, the lower is the roughening. This trend could already be observed in Figure 4c. However, the prominent peak at a spatial wavelength of 100 μm for a surface temperature of 290 °C is conspicuous. Here, the line feed of the meander raster path becomes apparent. Most probably, the forming residual layer shows an altered property at this temperature leading to the generation of ripples which correspond to the PJ line feed of 0.1 mm. According to the surface temperature measurement and the FEM simulation, there is a temperature range of about 220 °C to 330 °C over the entire optical element. Thus, most probably during the figure correction of the entire surface those features will also occur at certain positions where the critical temperature prevails. Due to the roughening in the range of spatial frequencies higher than 10^{-2} μm^{-1}, an additional surface smoothing step is subsequently required. Thereby, these features, having an amplitude of 10 nm (PV), should also be removed during this process.

Based on the previous results, the MRR is adjusted according to the temperatures resulting from the FEM simulation due to the geometry of the optical element. The normalized MRR, which is shown in Figure 11 as a two-dimensional graph and can be approximated by a 4th order polynomial in x and y direction with sufficient accuracy. Thus, in addition to the already determined nonlinear velocity dependence, the MRR variation as a function of local coordinates can also be integrated in the dwell time calculation in the form of a scaling factor.

Comparing the influences of both dependencies the non-uniform sample heating is more influential and leads to a reduction of the MRR of 25%. The velocity, on the other hand, causes the MRR to vary by only about ±3%, so its influence is comparatively small but nevertheless of importance not to be underestimated in high-precision figure error correction. Based on a surface form measurement, a figure error correction of the optical element was performed. The initial figure error is shown in Figure 12a.

The dwell time calculation results in a process time of about 3 h. During processing, the heater temperature was T_H = 500 °C. The plasma jet (see footprint profile in Fig. 12b) was moved in a meander path along the y direction and the line feed of 0.1 mm was executed along the x direction. After plasma processing the residual layer was removed by ultrasonic cleaning and another area measurement was performed. The resulting figure error is shown in Figure 12c. A prominent feature can be seen on the upper edge exhibiting a height of about 1 μm which was caused by a lateral workpiece alignment error. As a result, the figure error (rms) could only be halved in contrast to the previous calculation. Furthermore, it is noticeable that the power value (3rd Zernike polynomial coefficient) has

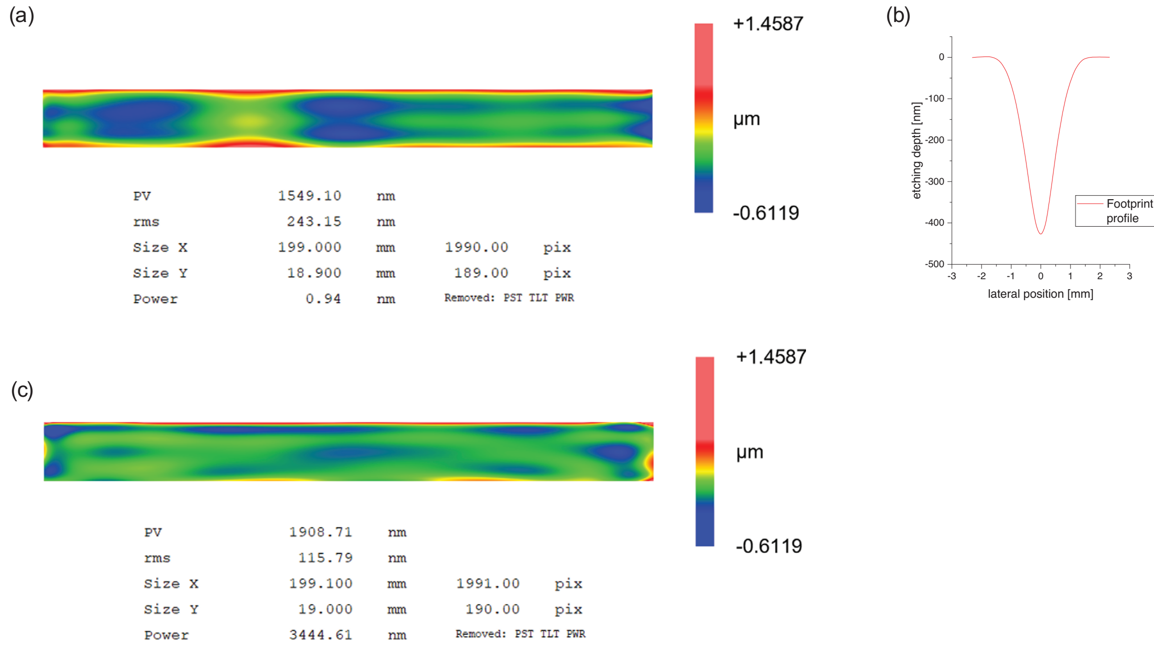

Fig. 12. Figure error of the optical element over the entire processing area (a) before PJM with (b) footprint profile (cross section of line etching for one line, $v = 1$ mm/s) and (c) figure error after PJM.

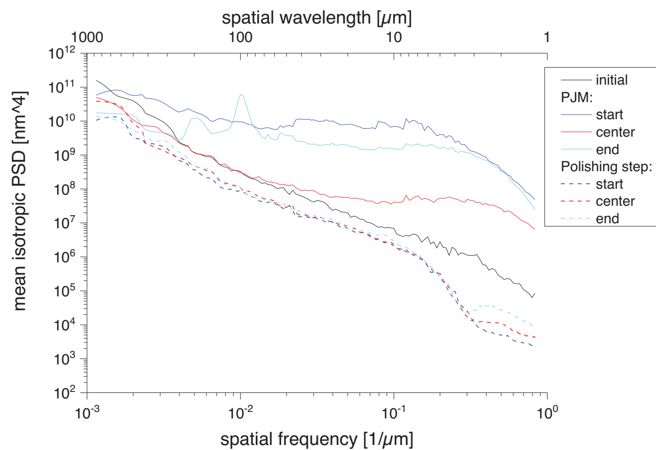

Fig. 13. Figure error correction of an optical element: isotropic PSD for defined points on the processed sample.

significantly increased to 3.3 µm indicating a global bow of the workpiece. It can be assumed that the optical element had some stress due to preliminary processes such as grinding and polishing, which is relaxed by the heating and the subsequent slow cooling cycle. In any case, the measurement of the normalized OPD effective value after processing did not show any birefringence caused by internal stresses.

Roughness measurements and the derived isotropic PSD function at different positions on the surface shown in Figure 13 reveal a similar roughening behavior as determined on the test samples. Roughness in the center is comparable to the studies of the partial area etching of the optical element (Fig. 8).

However, when looking at the roughness at about $x = \pm 100$ mm, there are significant differences. The removal depth which influences the roughness, as shown in Figure 4c, is about 1000 nm for the three measurement positions and therefore does not contribute to the significant difference. This is mainly driven by variations in surface temperature. At the beginning of the processing ("start", $x = +100$ mm), the total isotropic PSD is elevated compared to the initial surface indicating an increase of roughness over all spatial frequencies. This effect was also observed for a sample machined with PJ at a surface temperature of approximately 245 °C (compare Fig. 10b). The same surface temperature is present at $x = -100$ mm. Here, however, the temperature increase due to the moving PJ comes into play. At the end of the processing (at $x = -100$ mm), which lasted approx. 3 h, the optical element has most likely heated up successively due to the permanent contact of the PJ. Hence, the surface temperature T_S is probably higher than assumed from the results of the FEM simulation. The isotropic PSD measured at $x = -100$ mm shows a prominent feature at spatial frequency of 10^{-2} µm^{-1} caused by the raster path line feed of 0.1 mm similar to the PSD function shown in Figure 10b for $T_S = 290$ °C. It is thus deduced that the temperature of the optical element at this position was around 290 °C. As this temperature region seems to be critical for the development of ripple like structures, another workpiece heating setup that ensures sufficiently high surface temperatures should be considered in future experiments.

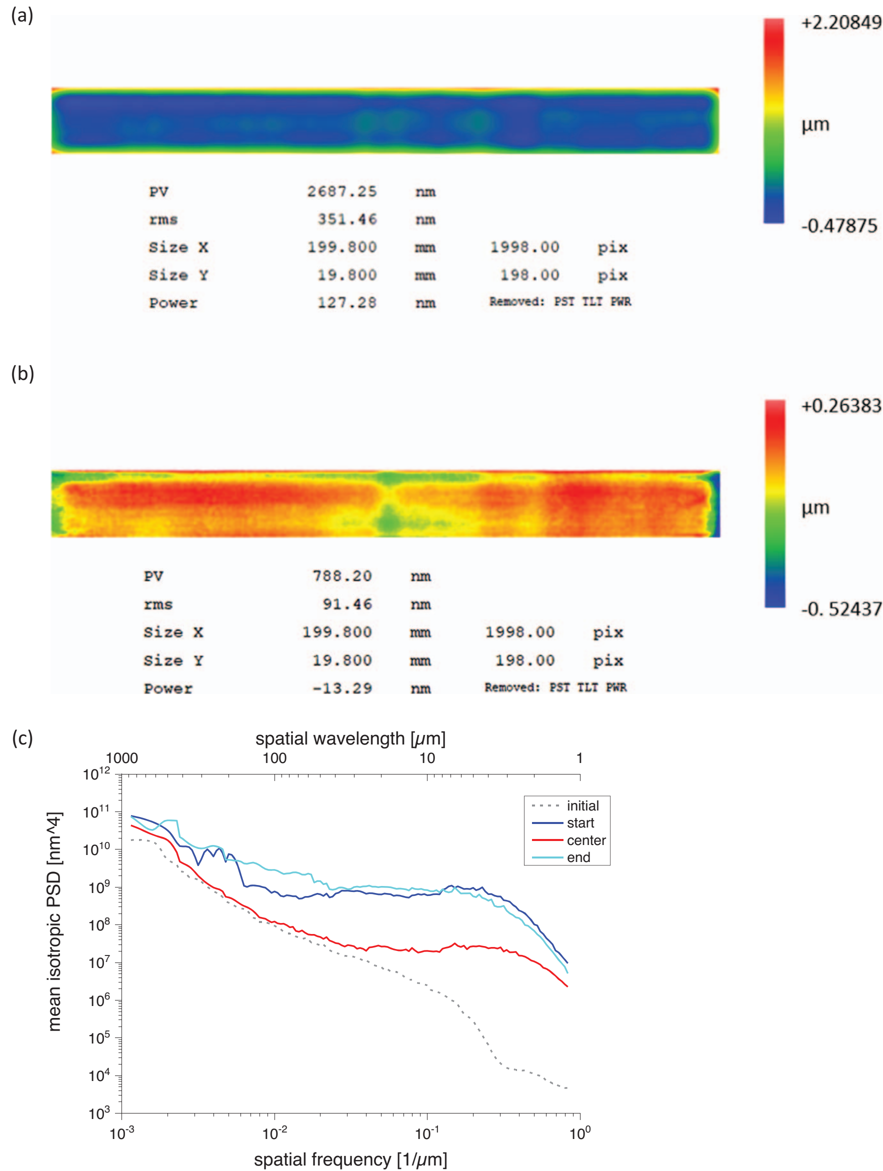

Fig. 14. Measurement of figure error of the optical element (a) before and (b) after the second PJ correction step and (c) calculation of the isotropic PSD for defined three well-chosen positions on the processed sample.

Due to the increased roughness after the figure error correction an additional mechanical-abrasive sub-aperture polishing step was required. The surface error increased from rms = 115.8 nm to rms = 351.5 nm, as can be seen in Figure 14a. Since polishing exerts mechanical forces to the surface by the polishing tool, the surface form deteriorates in the long spatial frequency range. However, the dashed lines in Figure 13 reveal that roughness was successfully reduced over the entire range of spatial frequencies. Especially, the prominent features caused by PJ processing have been completely levelled out. The isotropic PSD for the three measurement points are even depressed, compared to the initial surface.

A second PJM step was subsequently performed to further reduce form error using the same dwell time correction procedure as previously described. Hereby, the figure error was further decreased. To counteract the non-uniform global heating of the sample due to the heat input from the PJ, the line feed was performed here along the y direction. An areal measurement of the figure error after PJ processing is shown in Figure 14b. The form deviation can be reduced to less than 100 nm rms. For the clear aperture defined on the center area having dimensions of 195 mm × 15 mm, the figure error could even be reduced to 70.67 nm rms, which is a 74% form improvement.

The roughness shown as isotropic PSD in Figure 14c is comparable to the results of the first PJ correction step (see Fig. 13). The differences relate to the measuring position on the optical surface, which has the lowest roughness in the center, where the surface temperature has a higher value

compared to the position near the edges in x direction. Therefore, the surface at the outer positions exhibits a higher roughness. However, a noticeable feature at a spatial wavelength of 100 μm is no longer visible. Obviously, the modified PJ motion path leads to less asymmetric heating of the substrate and prevents the formation of ripple structures.

5 Conclusion

PJM to correct surface figure error of an optical element made of S-BSL7 was investigated. It was shown that the surface temperature has a significant effect on the MRR. In order to perform a deterministic correction process, the nonlinear dependence of motion velocity of the plasma jet as well as the characteristic surface temperature distribution on the MRR must be taken into account for the dwell time calculation. It has been demonstrated that figure error of an S-BSL7 optical element can be reduced by up to 74%. A global surface temperature of about 325 °C to 350 °C leads to a stable PJ etching process resulting in a uniform surface roughness. However, surface temperature below 300 °C leads to higher roughness. Consequently, more uniform heating of the substrate while maintaining the optimum surface temperature, *e.g.* by an optimized configuration of substrate heating, should be considered in future. Due to the increased surface roughness of the PJ processed surface, subsequent mechanical polishing is required. Minimizing the surface roughness reduces the polishing effort and results in less figure deterioration. Depending on the magnitude of initial figure error, iterative processing is proposed, including multiple cycles of PJM and polishing or smoothing.

Availability of data and materials

All data generated or analyzed during this study are included in this published article.

Conflict of interest

The authors declare that they have no competing interests.

Authors' contribution

HM conducted the PJ experiments, performed the analysis of the results and handled the paper documentation. TW provided the samples in the polished state and performed the optical measurement of the optical element after PJ correction. UB coordinated the work. GB supported the optical measurements of the optical element at the IOM and contributed important information to the interpretation and discussion with his expertise on the PJM. TA provided important information for the interpretation of the data, took extensive care of correction of the manuscript and provided valuable advice on presenting data more clearly. The authors have read and approved the final manuscript.

Acknowledgments. The authors want to thank T. Liebeskind for sample preparation. Further thanks go to F. Kazemi for the basic research on this topic during the last years. The project on which this report is based was funded by the German Federal Ministry of Education and Research under grant number 03WKCX1F. The responsibility for the content of this publication belongs to the authors.

References

1 Fischer L., Holder D., Krogmann S., Maier T. (2021) *Integration von Sensoren in das Exterieur-Design automatisierter/autonomer Fahrzeuge*, Fraunhofer-Institut für Arbeitswirtschaft und Organisation IAO, Stuttgart, p. 13. https://doi.org/10.18419/opus-11478.

2 VDI. (2019). *Automatisiertes und autonomes Fahren (VDI-Handlungsempfehlung)*. VDI, Düsseldorf.

3 SPECTARIS-Fachverband Photonik (2019) *Trendreport Photonik 2019/2020 – Märkte, Entwicklungen, Potenziale*, SPECTARIS Deutscher Industrieverband für optische, medizinische und mechatronische Technologien e.V., Berlin.

4 Rolland J.P., Davies M.A., Suleski T.J., Evans C., Bauer A., Lambropoulos J.C., Falaggis K. (2021) Freeform optics for imaging. *Optica* **8**, 2, 161–176. https://doi.org/10.1364/OPTICA.413762.

5 Yashchuk V.V., Rochester S., Lacey I., Babin S. (2020) Super-resolution surface slope metrology of X-ray mirrors, *Rev. Scientific Instrum.* **91**, 7, 075113. https://doi.org/10.1063/5.0005556.

6 Kazemi F., Boehm G., Arnold T. (2021) A novel Deal–Grove-inspired model for fluorine-based plasma jet etching of borosilicate crown optical glass, *Plasma Process Polym.* **18**, 3, 2000218. https://doi.org/10.1002/ppap.202000218.

7 Kazemi F., Boehm G., Arnold T. (2021) Recursive algorithm for modeling non-linear etching rates in reactive plasma jet based optical surface machining of borosilicate crown glass, *Precision Eng.* **72**, 205–214. https://doi.org/10.1016/j.precisioneng.2021.04.013.

8 Mogab C.J., Adams A.C., Flamm D.L. (1978) Plasma etching of Si and SiO_2 – The effect of oxygen additions to CF_4 plasmas, *J. Appl. Phys.* **49**, 7, 3796–3803. https://doi.org/10.1063/1.325382.

9 Kazemi F., Boehm G., Arnold T. (2019) Development of a model for ultra-precise surface machining of N-BK7® using microwave-driven reactive plasma jet machining, *Plasma Process Polym.* **16**, 12, 1900119. https://doi.org/10.1002/ppap.201900119.

10 Kazemi F., Boehm G., Arnold T. (2020) An investigation on effectiveness of temperature treatment for fluorine-based reactive plasma jet machining of N-BK7®, *Plasma Process Polym.* **17**, 8, 2000016. https://doi.org/10.1002/ppap.202000016.

11 OHARA GmbH (Ed.). (2021) *S-BSL7 Material Safety data Sheet*. Accessed: Mar. 23, 2021. [Online]. Available: https://www.ohara-gmbh.com/fileadmin/user_upload/export-data/pdf/security_datasheets/S-BSL7_English_.pdf.

12 Schott AG (Ed.). (2015) *Technical safety information N-BK7.* Accessed: Mar. 24, 2021. [Online]. Available: https://www.google.com/url?sa=t&rct=j&q=&esrc=s&source=web&cd=&ved=2ahUKEwjA5ued0-rzAhUJC-wKHYsoD4AQFnoECAYQAQ&url=https%3A%2F%2Fshop.schott.com%2Fmedias%2FN-BK7-SDS-EN-V5-201505.pdf%3Fcontext%3DbWFzdGVyfHJvb3R8OTQ2MDV8YXBwbGljYXRpb24vcGRmfGhmNy9oYzEvODgyMzM1Mzc3MDAxNC5wZGZ8YTIxZjdjNzIyOGUyNGI3MzljNmVkZjY4ZDliY2UzNDMwYTdlMTUxNmZjMWFmZTZiM2M1ZmY0ZmZmZDRmMWYwMw&usg=AOvVaw0a9ESojlBpNJ4WeV2NvAnZ.

13 Wiberg N. (2008) Lehrbuch der anorganischen Chemie, Walter De Gruyter & Co.

14 Lide D.R. (2004) *Handbook of chemistry and physics*, CRC Press LLC.

15 Lienhard J.H. IV, Lienhard J.H. V (2020) *A heat transfer textbook*, Phlogiston Press, Cambridge, MA.

16 Arnold Th, Böhm G., Paetzelt H. (2014) Ultra-precision surface machining with reactive plasma jets: ultra-precision surface machining with reactive plasma jets, *Contrib. Plasma Phys.* **54**, 2, 145–154. https://doi.org/10.1002/ctpp.201310058.

17 Su X., Ji P., Jin Y., Li D., Qiao Z., Ding F., Yue X., Wang B. (2021) Freeform surface generation by atmospheric pressure plasma processing using a time-variant influence function, *Opt. Exp.* **29**, 8, 11479–11493. https://doi.org/10.1364/OE.421688.

18 Arnold T., Boehm G., Eichentopf I.-M., Janietz M., Meister J., Schindler A. (2010) Plasma Jet Machining: A novel technology for precision machining of optical elements, *Vakuum in Forschung und Praxis* **22**, 4, 10–16. https://doi.org/10.1002/vipr.201000423.

19 Meister J., Arnold T. (2011) New process simulation procedure for high-rate plasma jet machining, *Plasma Chem. Plasma Process* **31**, 1, 91–107. https://doi.org/10.1007/s11090-010-9267-y.